Correction of JET bolometric maximum likelihood tomography for local gas puffing

OPEN ACCESS
IOP Publishing
Plasma Physics and Controlled Fusion
Plasma Phys. Control. Fusion **65** (2023) 075003 (11pp)
https://doi.org/10.1088/1361-6587/accd1c

Correction of JET bolometric maximum likelihood tomography for local gas puffing

Emmanuele Peluso[1,*], Andrea Murari[2,3], Teddy Craciunescu[4], Pedro Carvalho[5], Michela Gelfusa[1], Pasqualino Gaudio[1], Ivan Wyss[1] and JET Contributors[6]

[1] Department of Industrial Engineering, University of Rome 'Tor Vergata', via del Politecnico 1, 00133 Roma, Italy
[2] Consorzio RFX (CNR, ENEA, INFN, Università di Padova, Acciaierie Venete SpA), Corso Stati, Padova 35127, Italy
[3] Istituto per la Scienza e la Tecnologia dei Plasmi, CNR, Padova, Italy
[4] National Institute for Laser, Plasma and Radiation Physics, Magurele-Bucharest RO-077125, Romania
[5] Instituto de Plasmas e Fusão Nuclear, Instituto Superior Técnico, Lisbon 1049-001, Portugal

E-mail: emmanuele.peluso@uniroma2.it

Received 24 December 2022, revised 28 March 2023
Accepted for publication 14 April 2023
Published 23 May 2023

Abstract

Tomography is applied daily to bolometric data in magnetically controlled nuclear fusion devices to infer important quantities of the studied plasmas, such as the emissivity profiles or the radiated power in different locations of the main chamber. Tomographic reconstructions are also crucial for power balance analysis and to estimate heat fluxes for turbulence studies. One of the issues, associated with any tomographic technique, resides in the ill-posed nature of the mathematical problem, meaning that more than one possible emissivity profile is compatible with the measurements within the estimated uncertainties. Therefore, a careful evaluation of the quality of the obtained reconstructions is an important step of the analysis. On Joint European Torus (JET), since the two cameras are located in different toroidal locations, axial symmetry of the plasma radiation must be assumed to perform traditional tomographic reconstructions. Such a specific hypothesis, however, cannot be guaranteed in the case of symmetry-breaking mechanisms, such as strong local gas puffing for fuelling. The present contribution addresses this problem of local plasma fuelling, focusing on the observed significant mismatch between measured and back-calculated projections in specific pulses, including the last JET DT campaign (DTE2) carried out in 2021. The analysis indicates that the observed discrepancy, due to the gas injected primarily from valves located in the same octant where one of the bolometer arrays is located, can be rectified acceptably well by a physically-based correction. The sensible improvements in the bolometric maximum likelihood tomography's outputs are also

[6] See the author list of 'Overview of JET results for optimising ITER operation' by J Mailloux *et al* to be published in *Nuclear Fusion Special issue: Overview and Summary Papers from the 28th Fusion Energy Conference* (*Nice, France, 10–15 May 2021*).

[*] Author to whom any correspondence should be addressed.

documented, and the possible physical explanation for such a phenomenon is discussed. The study performed in this article is expected to have a significant impact on the analysis of JET data and on the physical interpretation of the results obtained during the recent DTE2 experiments, for which a proper evaluation of the radiated power estimates is of non-negligible relevance.

Keywords: bolometry, tomography, maximum likelihood, nuclear fusion, turbulence and transport, optimization

(Some figures may appear in colour only in the online journal)

1. Introduction

Tomographies are routinely applied to data collected from magnetically confined thermonuclear plasmas to perform indirect estimates of important physical quantities. Such a technique is based on the measured integrated signals (projections) of the plasma emissivity along viewing cones (lines of sight, i.e. LOSs). It is an inverse severely ill-posed problem, basically meaning that multiple solutions are compatible with the measurements.

On the Joint European Torus (JET), tomographies are used to investigate the total radiation of the plasma, MHD instabilities and impurity transport [1–4], as well as neutron emission [5, 6] and fast particles (via gamma ray emission) [6, 7]. Naturally, different ranges of energies and physical phenomena are investigated via different detectors: (a) metal foil bolometers (near-infrared to Soft X-rays (SXRs)) [8], solid-state detectors (SXRs and gammas) [9], liquid and plastic scintillators (neutrons and gammas) [10].

With regard to bolometric algorithms at JET [3, 4], the maximum likelihood (ML), the minimum Fisher regularization and a neural network (NN)-based approach have been recently implemented to complement the already available codes [1]. The just cited techniques use a regularization procedure, each one based on a different statistical principle. The only exception is the NN approach [11], since it is not an actual tomographic algorithm (but a network trained to reproduce one) that does not use any direct optimization.

In general, however, one strong hypothesis behind any tomographic code is related to the assumption that the emissivity is toroidally symmetric, and therefore it can be sampled on any poloidal plane. Naturally, such a hypothesis cannot be fulfilled in principle because of gas puffing, but on JET, a further difficulty exists since the two main arrays of bolometers (KB5H and KB5V) lay on two different octants [8], as shown schematically in figure 1. Consequently, puffing between the two arrays, or even close to one of them, might influence the measurements and then the tomograms from which estimates are derived.

In preparation for the most recent DT campaign carried out in 2021, referred to as DTE2 from now on, specific valves have been installed on JET, called tritium introduction moduli (TIMs) to match the DTE2 requirements [12] in addition to the already installed gas introduction moduli (GIMs) in the torus.

In more detail, the valves used for the main chamber flow (MCF) of interest in the study reported here are TIM15 and GIM03, the closest valves to the horizontal array of bolometers, while TIM/GIM07 are located on the top of the same octant. Moreover, between the two octants, different valves have also been used in DD operations for puffing. Among them, only GIM06 is located on the top of the fourth octant [12], i.e. between the two octants of the arrays of bolometers. On JET, four GIMs and three TIMs are also installed in the divertor (DIV) region and can also be used for specific tasks, such as impurity seeding, minority injections, X-point control and landing, for example. Moreover, their proximity to the cryogenic pumps sensibly reduces their fuelling efficiency [12]. This is the reason why only the previous MCF listed valves have been considered in this article. The aforementioned moduli are schematically reported in figure 1. A more comprehensive description can be found in the literature [12].

It has been known since the installation of certain TIMs that they could influence bolometric measurements [13]. Their frequent use during the DTE2 campaign required the application of an ad hoc correction based on a shot-to-shot basis. No general correction has been found, however. This article is therefore devoted to providing a physically-based correction and a dedicated methodology to be applied automatically to the horizontal LOSs.

It has to be stated that the technique reported in this article can be implemented in any iterative algorithm, but it has been derived and tested using the ML one: the iterative approach that has already been demonstrated to be able to provide accurate, reliable reconstructions with estimates of the confidence intervals associated with the reconstructed emissivity profiles and derived quantities.

A wrong estimate of the emissivity profiles and of the radiation density profiles can affect many derived quantities and studies, such as: (a) transport studies (including impurity ones); (b) MHD analysis, which is also strictly connected with the transport; and (c) disruption avoidance studies, which are linked to both MHD, transport and radiation.

Profiles are indeed relevant for the electron energy balance, thus influencing the transport channels [14], and therefore can be used, for example, as input to dedicated codes, such as TRANSP [15]. Furthermore, with regard to impurities and their transport, radiation profiles are intrinsically related to the impurity density profiles, which have a strong impact, again, on both confinement and disruptions [14].

The structure of this article is as follows: section 2 summarizes the JET bolometric systems and recalls the main hypothesis behind the inversion methodology followed in this

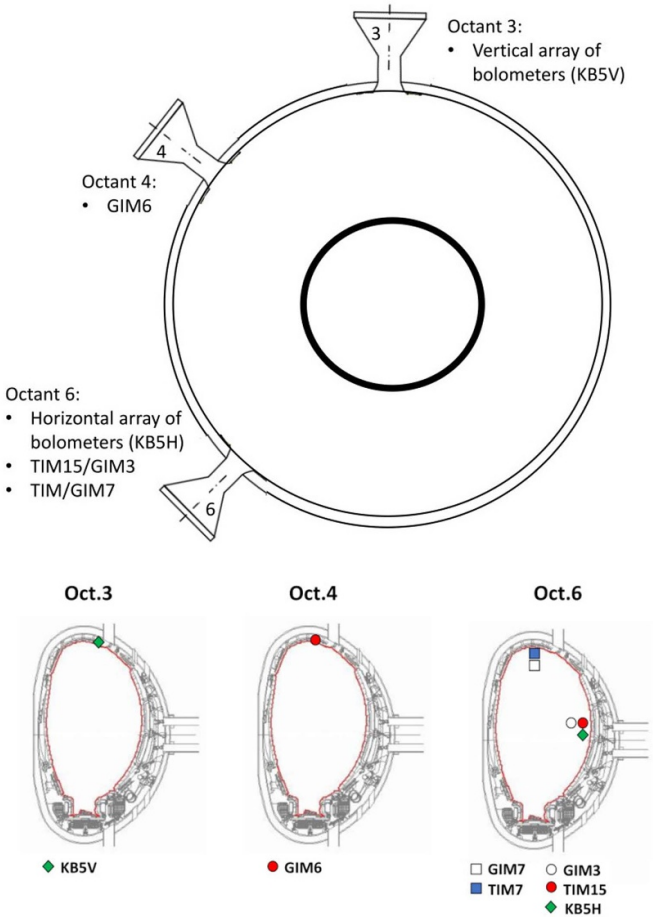

Figure 1. Top: spatial location of the MCF valves considered in this article (GIM3/6/7, TIM07/15), located either in the midplane or on the top of the corresponding octant. The two bolometric arrays are also listed in the third (KB5V) and sixth (KB5H) octants. Bottom: schematic plots reporting, for each octant, the poloidal locations of the just cited valves and arrays of bolometers.

article, i.e. the ML approach. In section 3, a pure empirical correction for the horizontal LOSs in terms of the injected electron flow rate $\left(\phi\left[\frac{\text{electrons}}{\text{s}}\right]\right)$ called the flow-ratio-based correction is introduced first. A more advanced model to derive a more general correction, based on the ratio of the emissivities in two different regions of the main chamber, is described next. An iterative procedure is also presented in the same section to fine tune the emissivity-ratio-based correction. Section 4 shows significant examples of DT and DD pulses to highlight the relevance of the corrected estimates provided by the suggested correction and algorithm in different areas. The last section is then devoted to the conclusions.

2. Maximum likelihood (ML) at JET

This section comprises two subsections: the first is devoted to the bolometric systems on JET, and the second describes the main features of the ML approach, leaving the details to the cited references.

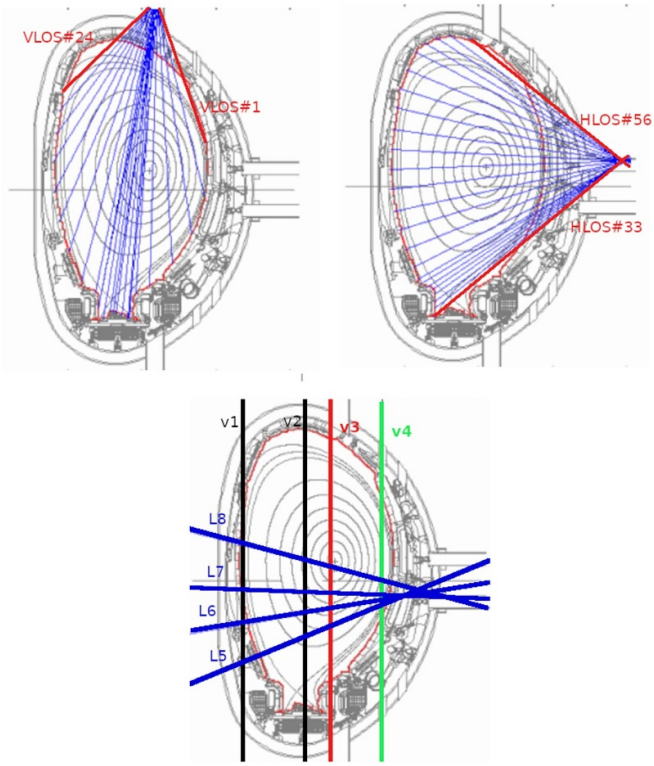

Figure 2. Top left: LOSs of the vertical KB5 array of bolometers located in the third octant; top right: LOSs of the horizontal KB5 array of bolometers located in the sixth octant. In both pictures the first and last LOSs have been highlighted in red to mark the sequence; bottom: interferometer LOSs, where the chords considered for the edge and the core in this article have been reported in green (v4) and red (v3), respectively.

2.1. JET bolometers

Bolometers at JET are 8 μm tick gold-foil absorbers, with a flat sensitivity from 0.1 nm ($\sim$10 keV) to 480 nm ($\sim$2.5 eV), i.e. from the near-infrared to SXR [16].

They are divided into two arrays, as reported in figure 2 on top, each consisting of 24 LOSs: the vertical (KB5V) array is located in the third octant, and the horizontal one (KB5H), in the sixth octant [8]. The data have a sampling rate of 5 kHz, and are usually averaged over 25 ms to perform a tomographic reconstruction. The time window cannot be shorter than 5 ms because of hardware filters in the signal processing chain to reduce the effect of noise.

2.2. Overview of the ML approach and of the expectation maximization algorithm for tomography

The ML approach was originally developed for gamma and neutron tomography [6] on JET and more recently applied to bolometry on JET [2] and AUG [17]. In the following notation, either vectors or matrices will be implicitly denoted by a bold letter.

The general computerized tomography of ML is well described in the literature [18–21] and is based on the

hypothesis that both the 'n' pixel (*voxel*) of the poloidal emissivity distribution $\boldsymbol{f} = f_n$ and the measurements $\boldsymbol{g} = g_m$ collected by 'm' detectors follow Poisson statistics [22]. The conditional probability of detecting $\boldsymbol{g}$ measurements by the emissivity profile $\boldsymbol{f}$ can therefore be written in the form of the likelihood:

$$L(\boldsymbol{g}\,|\boldsymbol{f}) = \prod_m \frac{1}{g_m!}(\overline{g_m})^{g_m} \times \exp(-\overline{g_m}) \tag{1}$$

where the $\overline{g_m} = E\{g_m|\boldsymbol{f}\}$ stands for the conditional expectation value of g_m events collected by the detector m, given $\boldsymbol{f}$, the emissivity profile. The ML is then implemented via an expectation maximization (EM) algorithm to converge on an estimate $\boldsymbol{f}_{\boldsymbol{ML}}^{(\boldsymbol{k}^*)}$ of $\boldsymbol{f}$. The geometry of the LOSs and the etendues of the bolometers allow one to estimate the matrix $\mathbf{H}$, describing for each voxel ($H_{\boldsymbol{mn}}$) the contribution to each LOS of the power radiated by the voxel itself. Using the same terminology as [20], one can write [20]:

$$\overline{g_m} = \sum_m H_{mn} f_n \tag{2}$$

and the iterative procedure can be summarized by the following formula:

$$f_n^{(k+1)} = \frac{f_n^{(k)}}{\sum_m H_{mn}} \sum_m \left(g_m \Big/ \sum_j H_{mj} f_j^{(k)} \right) H_{mn} \,. \tag{3}$$

Equation (3) is used to update the 2D profile until a convergence criterion is satisfied [19] at the iteration k^* and, therefore, $\boldsymbol{f}^{(\boldsymbol{k}^*)} = \boldsymbol{f}_{\boldsymbol{ML}}^{(\boldsymbol{k}^*)}$.

The initial guess can be either uniform or a specific mask [23]. The latter approach has been demonstrated to drastically reduce the occurrence of artefacts in the core region or close to the upper dump plates on the high-field side, while the former is mathematically simpler and faster to evaluate. The ML approach also has the advantages of estimating the covariance matrix $\boldsymbol{K}_{\boldsymbol{ML}}^{(k^*)}$. Therefore, for each 2D emissivity distribution, an estimate of the uncertainty associated with each voxel can be provided. Details can be found in [2, 20].

As a general consideration, it is important to recall that the image of the uncertainties for each emission profile resembles the profile itself. This is due to the non-linearity of the variance estimate [20] and, therefore, it is in contrast with linear reconstruction methods, where bright features contribute to distant and low-intensity regions. Based on $\boldsymbol{K}_{\boldsymbol{ML}}^{(k^*)}$, the uncertainties related to each derived quantity can therefore be estimated, thus providing the confidence intervals.

To conclude the paragraph, the algorithm implemented at JET uses the smoothness along magnetic surfaces as the only regularization criterion. At the same time, the procedure can also take into account the most important sources of errors on the measurements, such as outliers, faulty LOSs and uncertainties on the spatial estimates of the magnetic surfaces [24, 25].

The following section is devoted to introducing the empirical correction and its extension, based on a simplified model linking the relative importance of the emissivity per unit volume, frequency and solid angle in two regions of the main chamber containing the plasma.

3. Simplified model of the problem

This section is divided into three subsections. In section 3.1, an interpretation of the outputs observed by a direct application of the ML algorithm is reported using a phantom. In section 3.2, a physically-based correction is described, while in section 3.3, a complete methodology for its application is reported.

3.1. Interpretation of the ML outputs in a symmetry-breaking mechanism

As mentioned in the introduction, due to gas puffing, the symmetry of the problem is broken, and therefore the two arrays of bolometers detect a different power as if the emissions on the two poloidal planes were different. Indeed, the outputs of the ML code for contaminated data, as reported, for example, in figure 3(E) for a *phantom* and in figures 4(C)–(I) for an experimental case, show an evident misfit between the measured and the back-calculated projections.

According to equation (3) then, the ML algorithm iteratively adjusts the emissivity of a voxel 'j' $\left(f_{n=j}^{(k+1)}\right)$. This is done by averaging the values of the back-calculated projections interested by the pixels considered, using the ratio of the measures g_m and the projections at the previous iteration $\sum H_{mj} f_j$.

Taking into account the layout of the diagnostic, each voxel actually refers to two different elementary plasma volumes, each located in a different poloidal plane of two different octants.

For the sake of simplicity, it can be assumed that such a voxel 'j' is covered by a pair of LOSs, one per camera array. By now considering a specific event breaking the toroidal symmetry, the puffing, it can be assumed that only the measured brightness of the horizontal camera LOS would actually be affected. The code would then iteratively tend to match the measured brightness on this set of LOSs, by overestimating the back-calculated measures of the other camera. This explanation has been tested on a phantom and is clearly in line with the results reported in figure 3. It can be seen how the algorithm can properly reconstruct (figure 3(B) and projections in figure 3(D)) the created phantom (figure 3(A)) in the absence of any symmetry-breaking events, or in the case of a proper correction. In contrast, if the horizontal projections (from 33 to 56) are altered by a scale factor, as in figure 3(E), the EM algorithm tries to compensate the asymmetric brightness, producing the wrong reconstruction of the phantom, as shown in figure 3(C).

The phantom reported in figure 3 has been chosen since it provides similar behaviour w.r.t. the experimental observations reported in the following sections.

Before describing the implemented corrections in the following subsection, it is important to mention that, to disentangle the possible effect of valves located between the two

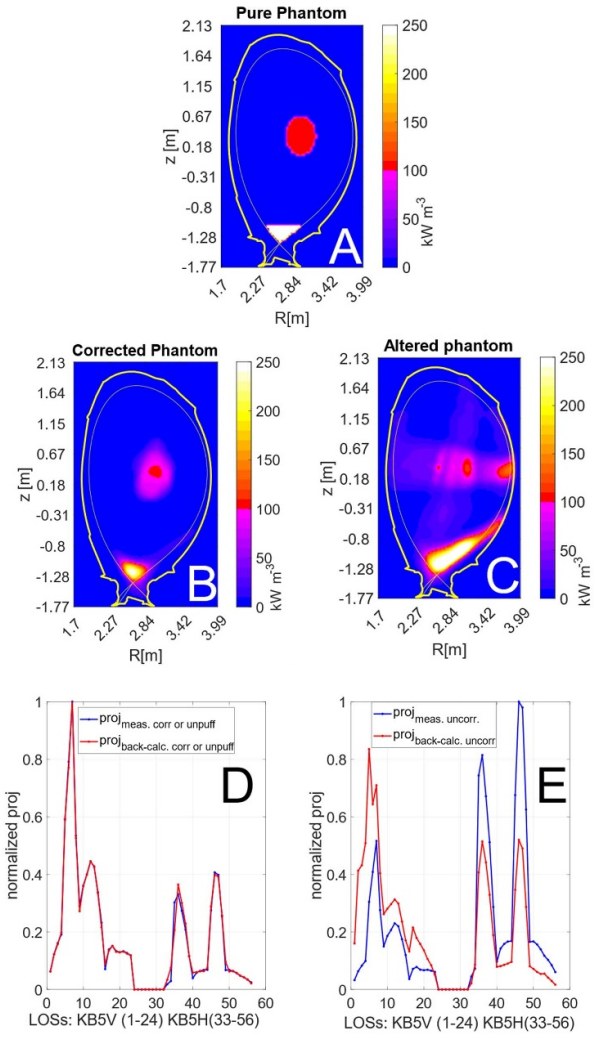

Figure 3. (A) A created phantom. (B) A reconstructed phantom by the ML algorithm corresponding to projections in (D), where measurements have been corrected by the same scaling factor used in (E) to only alter the KB5H LOSs; (C) a tomogram of the emissivity profile once only the horizontal LOSs (from 33 to 56) have been multiplied by a scaling factor, as shown in (E), where the behaviour of the ML code, that is trying to compensate the asymmetric brightness, can be clearly observed and is compatible with observations in figures 4(C), (I).

octants and those located in the same octant of KB5H, selected pulses have been analysed for which only the GIM06, i.e. the main valve located between the two arrays of bolometers, was used. The pulses investigated had up to 95% of the total flow rate puffed in the main chamber by GIM06, and the results have shown a negligible influence since no correction was actually needed because the EM algorithm was able to converge on a reliable estimate of the back-calculated projections, with a reduced chi-square $\left(\frac{\chi^2}{\nu}\right)$ comparable to that obtained by applying any correction. This implied that the symmetry of the problem could be maintained in the gas puffing from GIM06.

At the same time, confirming the influence of the valves located close to or in the same octant as KB5H, a similar analysis has been performed by considering a shot, in which GIM03, located close to TIM15, provided up to 98% of the total fuelling. The effect on KB5H was similar to that observed in figure 3(E) or figures 4(C)–(I). Finally, it has been observed how TIM15 and GIM3 have, in general, a strong effect on all the KB5H LOSs, while the influence of TIM/GIM7 can be confined more often to the most peripherical horizontal LOSs instead.

The next subsection is dedicated to describing the 'flow-ratio-based correction', called FRC from now on, and a more general one, based on a simplified physics model: the 'emission ratio correction' (ERC).

3.2. FRC and ERC corrections

In this subsection, a simplified model is described to estimate a scalar value to correct the bolometric measurements in a non-negligible symmetry-breaking event due to strong gas puffing. Such a correction generalizes a pure empirical correction that will be discussed first.

The fundamental idea underlying the derived correction relies on assuming that the measured brightness of affected bolometers is not only due to the toroidally symmetric emission of the plasma, but it might also be correlated to the local puffing of the MCF valves located between the two octants in which the cameras are installed and, even more strongly, from those placed in the same octant of the cameras themselves.

Consequently, to test the hypothesis of a local influence of strong puffing on the bolometric measurements, a pure empirical correction had initially been implemented, based on the ratio between the electron flow rate puffed by the MCF valves (GIM6, GIM3, GIM/TIM7, TIM15) located between the two octants, where the bolometric cameras are installed over the total puffed electron flow rate. Such a correction (α_0) had been applied in the first instance to KB5H measurements $(\mathrm{KB5H}_m)$ as:

$$\boldsymbol{KB5H} = \boldsymbol{KB5H} \cdot (1 - \alpha_0)$$
$$\text{where } \alpha_0 = \frac{\sum_{1=1}^{5} \phi_i}{\phi_{\mathrm{tot}}}. \tag{4}$$

In equation (4) ϕ_i stands for the electron flow rate of the MCF valve considered, assuming $i := \{\mathrm{GIM3}, 6, 7, \mathrm{TIM7}, 15\}$, while ϕ_{tot} stands for the total electron flow rate of the pulse considered. Therefore, $\sum_{1=1}^{5} \phi_i$ is lower, in general, w.r.t. the total flow rate, because it includes only the contribution of the MCF cited above. However, for specific discharges or time windows, it may represent the total electron flow rate ϕ_{tot}.

For most pulses such a correction compensates the contaminated measurements quite well. An exemplificative time instance is shown in figures 5(C) and (D), where the behaviour of the FRC is shown. In figures 5(A) and (B) instead, the ERC is reported for comparison. The emission patterns (figures 5(D) and (B)) are indeed similar $\left(\frac{P_{\mathrm{rad}}^{\mathrm{FRC}}}{P_{\mathrm{rad}}^{\mathrm{ERC}}} \simeq 1.06\right)$, as well as the overall behaviour of the back-calculated projections in the two cases (FRC in figure 5(C), and ERC figure 5(A)). The total and the electron flow rates from the

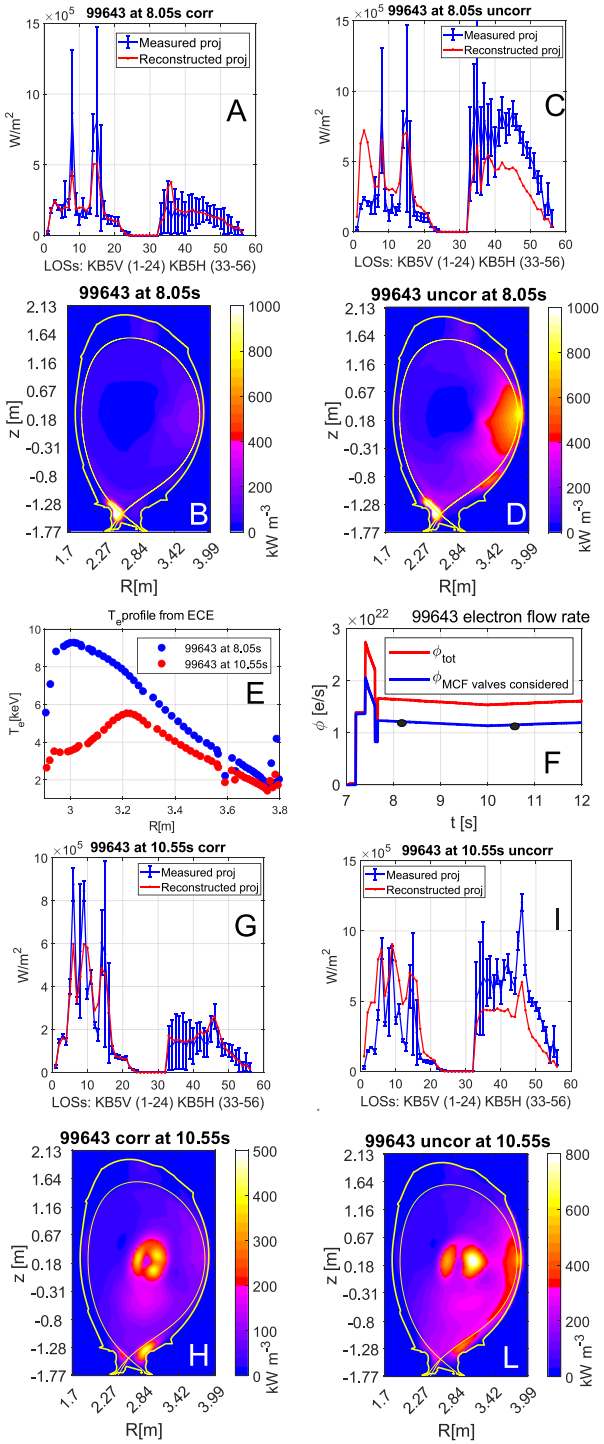

Figure 4. Exemplificative time instances of the DT discharge 99 643: measured and back-calculated projections once the correction has been applied (A), (G) or not (C), (I); (B), (H) and (D), (L) show instead the tomograms of the emissivities obtained in the two cases. Figures (A), (B) and (C), (D) correspond to a centrally peaked temperature profile (reported in blue in (E)) at 8.05 s $\left(\alpha_{1f}^{99643}\left(t=8.05\,\mathrm{s}\right)\simeq 0.15;\ \alpha_{1f}^{99643}\left(t=10.55\,\mathrm{s}\right)\simeq 0.21\right)$, while (G), (H) and (I), (L) stand for the reconstructions at 10.55 s with a hollow electron profile (reported in red in (E)). The main plasma parameters in terms of I_p, B_t, (n_e^c, T_e^c) and (n_e^e, T_e^e) are reported: 99643 : $\left[\left(2.3\ \mathrm{MA}, 2.5\ \mathrm{T}, \left(4.7\cdot 10^{19}\mathrm{m}^{-3}, 3.1\ \mathrm{keV}\right),\right.\right.$ $\left.\left.\left(2.7\cdot 10^{19}\mathrm{m}^{-3}, 1.1\ \mathrm{keV}\right)\right)\right]$.

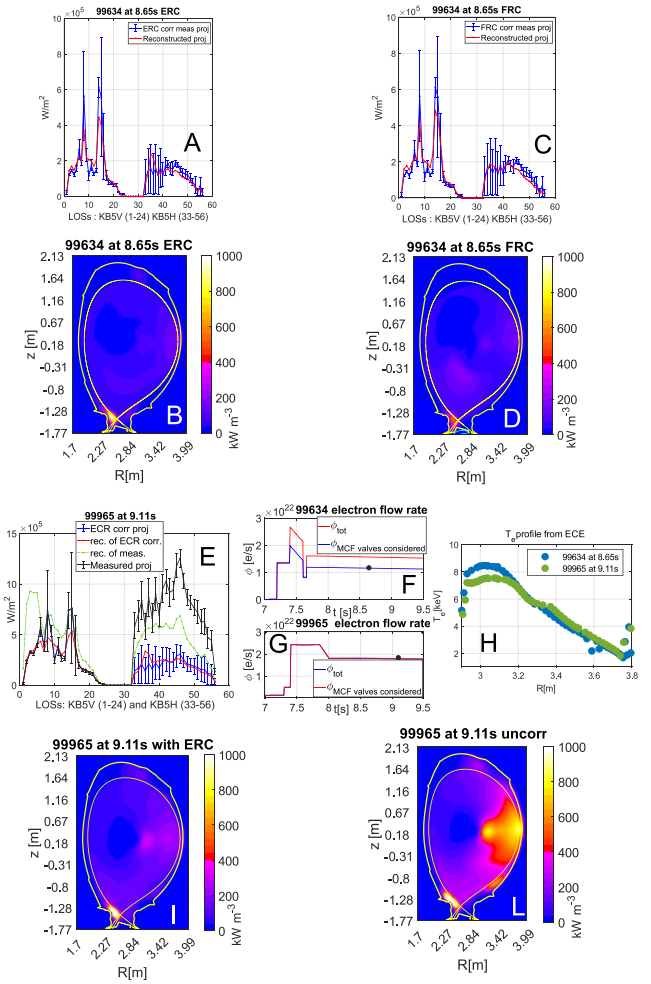

Figure 5. Exemplificative time instances of the DT discharges 99 634 (A), (B), (C), (D) and 99 965 (E), (I), (L). (A), (B): ERC corrected measurements at 8.65 s for the 99 634 case $\left(\alpha_{1f}^{99634}\left(t=8.65\ \mathrm{s}\right)\simeq 0.23\right)$; (C), (D): FRC corrected measurements $\left(1-\alpha_0^{99634}\left(t=8.65\ \mathrm{s}\right)\right)\simeq 0.26\big)$. The emission profiles are similar, as are the back-calculated projection profiles, confirming the generally good compensation of the FRC. (E): uncorrected (black) and ERC corrected (blue) measurements with the corresponding back-calculated projections (in green and red, respectively) for the 99 965 pulse at 9.11 s for which the FRC could not be applied; in this case $\alpha_{1f}^{99965}\left(t=9.11\ \mathrm{s}\right)\simeq 0.24$. (F) and (G): in red, the total electron flow rate and, in blue, the electron flow rate from the MCF valves that are relevant for this study. The two estimates may overlap, as for the 99 965 case for the time interval shown, thus stressing the importance of the ERC correction. The time instances considered have been marked in black for both pulses; (H) ECE profiles; (I) the ERC corrected tomogram; (L) the tomogram obtained from uncorrected measurements (no correction applied). The main plasma parameters in terms of I_p, B_t, (n_e^c, T_e^c) and (n_e^e, T_e^e) are reported 99634 : $\left[\left(2.5\ \mathrm{MA}, 3.4\mathrm{T}, \left(4.4\cdot 10^{19}\mathrm{m}^{-3}, 7.5\ \mathrm{keV}\right),\right.\right.$ $\left.\left.\left(2.5\cdot 10^{19}\mathrm{m}^{-3}, 1.3\ \mathrm{keV}\right)\right)\right]$ 99965 : $\left[2.3\mathrm{MA}, 3.1\mathrm{T}, \left(5.2\cdot 10^{19}\mathrm{m}^{-3},\right.\right.$ $\left.\left.6.7\ \mathrm{keV}\right), \left(2.9\cdot 10^{19}\mathrm{m}^{-3}, 873\ \mathrm{eV}\right)\right]$.

valves considered in this analysis are shown in figure 5(F) instead.

The FRC has, however, some limitations that are mostly related to the discharges in which only the aforementioned

valves between the bolometric cameras are used to fuel the plasma, i.e. when $\Sigma\phi_i \sim \phi_{\rm tot}$, resulting in a dummy α_0 equal to '1'. Figure 5(E) shows an exemplificative time instance at which the FRC could not be applied for this reason, while the ERC could be estimated instead. Figure 5(G) shows, in fact, the electron flow rates of the aforementioned MCF valves used in the pulse, GIM07 and TIM15, whose electron flow rates sum up to the total injected one for the time instance considered (highlighted by the black full dot).

Figure 5(H) shows the ECE profiles for completeness. Figure 5(I) provides the tomogram corresponding to the ERC corrected measurements, reported with blue dots and bars in figure 5(E). Figure 5(L) instead shows the uncorrected case, corresponding to the black dots and bars in figure 5(E).

The good behaviour of the just described empirical correction FRC, proportional to the puffed flow rate ratio, suggests therefore the possibility of defining a more general formulation of the correction itself in terms of fundamental plasma quantities. This also can tackle the limitations just described. Therefore, the following simplified model has been derived.

By considering the plasma emissivity as the sum of two contributions:

$$\epsilon_u^c + \epsilon_u^e = \epsilon_u^{\rm tot} \tag{5}$$

where the subscript 'u' stands for *unaltered*, referring to the emissivity that could be observed by steady ion charge states in the plasma, i.e. in the absence of significant particle puffing, both in the central region ('c') or in the edge of the plasma ('e').

Assuming, on the other hand, that the estimates of the emissivities can be derived from the plasma parameters in both macroscopic regions, it is possible to define the *measured* ones, consequently labelled as $\epsilon_m^{c,e}$
Finally, the following order is imposed:

$$\begin{aligned} &\epsilon_u^c \simeq \epsilon_m^c \\ &\epsilon_u^e = \alpha_1 \epsilon_m^e \text{ with } \alpha_1 \leqslant 1 \end{aligned}. \tag{6}$$

In equation (6) it has been supposed that the *unaltered* emissivity from the central part of the plasma is almost the measured one, i.e. it is not affected by the puffing. Instead, in the edge region, it is actually lower w.r.t. the one that can be estimated from the measurements, by a factor 'α_1' that has to be lower or equal to one. Therefore, the following inequality can be written:

$$\epsilon_u^c + \epsilon_u^e = \epsilon_u^{\rm tot} \leqslant \epsilon_m^{\rm tot} \simeq \epsilon_m^e \tag{7}$$

where it has also been assumed that, because of puffing, the periphery dominates the magnitude of the emissivity. Then, by considering equation (7) and the system in equation (6) it is possible to converge on:

$$\alpha_1 \leqslant \left(1 - \frac{\epsilon_m^c}{\epsilon_m^e}\right) \quad . \tag{8}$$

By taking the maximum of equation (8), i.e. assuming $\alpha_1 = \left(1 - \frac{\epsilon_m^c}{\epsilon_m^e}\right)$, it is therefore expected that the actual correction can be lower or equal than the maximum considered as the initial guess. The following step consists of assuming that the correction derived in equation (8) can be applied to the affected LOSs in the first instance, instead of the emissivity of a specific region of the plasma, i.e:

$$\boldsymbol{KB5H} = \alpha_1 \boldsymbol{KB5H} \quad . \tag{9}$$

The last steps for deriving a correction factor consist of defining an approximate expression for α_1 and defining a methodology to converge on a fine-tuned correction, adjusted to the data, according to equation (8).

The details with regard to how the ERC correction in equation (8) has been estimated and how it has been implemented are reported in the following subsection.

3.3. Practical implementation of the ERC correction

The evaluation of the ratio $\frac{\epsilon_m^c}{\epsilon_m^e}$ shown in the previous section would, in principle, require an accurate analysis of the concentrations of impurities [26] as well as their dynamics [27]. This is used to estimate the relative contribution of line radiation, recombination processes (radiative and dielectronic recombination), charge exchange [28, 29] and free–free (Bremsstrahlung) emissions both in the core and at the edge of the plasma. Such an analysis would not be a realistic option if the correction is to be applied to a large number of pulses and in an automatic way.

Therefore, considering equation (9) and assuming the plasma is in a coronal equilibrium, the ratio reported has been approximated by the following expression:

$$\alpha_1 = \left(1 - \frac{1}{Z_{\rm eff}} \left(\frac{n^c}{n^e}\right)^2 \sqrt{\frac{T^e}{T^c}}\right). \tag{10}$$

In equation (10), approximated expressions for the emissivities per unit volume, solid angle and photon energy have been used [30–32]. The previous equation can be read as if, for the core term, the bremsstrahlung was the dominating mechanism. Instead, for the edge, recombination is the main physical mechanism considered. In equation (10), $n^{e,c}$ and $T^{e,c}$ stand for the electron densities and electron temperatures at the edge and core, respectively.

The approximated Bremsstrahlung term then reads as [31]:

$$\epsilon_m^c|_{\rm Bremss.} \approx \frac{n_e^2}{\sqrt{T_e}} Z_{\rm eff} \bar{g}_{ff} e^{-\frac{h\nu}{T_e}} \approx \frac{n_e^2}{\sqrt{T_e}} Z_{\rm eff} \tag{11}$$

where the only quantity depending on the atomic physics is $\bar{g}_{ff}$, the temperature averaged Gamov free–free term. To properly consider the recombination instead, the contribution of each species should in principle be considered, both in terms of their nature and of their ionization states, especially for impurities. Such a dedicated analysis would go beyond the scope of the present study, and would not be compatible with corrections

to be routinely applied. Equation (12) then reports the approximated term considered [31, 32]:

$$\epsilon_m^e|_{\text{Recomb.}} \approx \frac{n_e}{\sqrt{T_e}} \sum_i n_i Z_i^2 \beta\left(Z_i, T_e\right) \left(\bar{g}_{fb}\right)_i e^{-\frac{h\nu}{T_e}} \approx \frac{n_e^2}{\sqrt{T_e}} Z_{\text{eff}}^2 \tag{12}$$

where n_i stands for the density, with charge Z_i, of the ion species 'i' considered, $\left(\bar{g}_{fb}\right)_i$ is the free-bound Gaunt factor averaged over the states of a given principal quantum number 'n' and the term $\beta\left(Z_i, T_e\right)$ has been approximated by keeping only its dependence on Z_i^2 to stress the overall one on $\sim Z^4$, i.e. on $\sim Z_{\text{eff}}^2$.

It can also be seen how the free-bound and free–free Gaunt factors, ranging from 2 to 5 in the visible range to 1 in SXR, as well as the photon energy term have been neglected to obtain equation (10).

Strong assumptions have been made, but at the same time, the derived non-dimensional correction can be roughly justified assuming that recombination is dominant because of the gas influx due to the puffing valves and the contribution from impurities due to Be influxes from the wall, and to Ni sources in the mid-plane or to W from the divertor [26]. On the other hand, neglecting the recombination of heavy ion contribution to the continuum in the core can be justified by the fact that such ions radiate in the SXR region, where the bolometers are almost blind [16].

To estimate the most reliable tomogram then, the following procedure has been implemented.

(a) Estimate of the ERC initial guess α_1;
(b) Application of α_1 to the most peripherical LOSs of the horizontal camera (KB5H) looking at the upper dump plates;
   1. Calculation of the reduced chi-square $\frac{\chi^2}{\nu}$ for all the $\nu =$ 24 KB5H LOSs;
   2. Iteration of the procedure by correcting α_1 with a multiplication factor δ proportional to the misfit between the corrected measurements and the back-calculated ones until $\frac{\chi^2}{\nu} \leqslant \chi^2_{\text{lim}}$; where the suggested value for χ^2_{lim} is one;
   3. If $\frac{\chi^2}{\nu}$ does not fall below the χ^2_{lim} set after $n = 3$ iterations, move to point (c);
(c) Application of α_1 to all LOSs (24) of the horizontal camera (KB5H), because of the actual proximity of the interested MCF valves to the camera;
   1. Application of the iterative procedure described in (b1), (b2), (b3), referring this time to all the channels of the horizontal camera. In case $\frac{\chi^2}{\nu}$ will not fall below the χ^2_{lim} set again, after $n = 3$ iterations, move to point (d), otherwise to point (e);
(d) Increase the χ^2_{lim} originally set and repeat from point 1. In case the $\frac{\chi^2}{\nu}$ will not fall below the maximum allowed $\chi^2_{\text{limMAX}} = 3.84$, then the uncertainty on the measurements is increased from one to three standard deviations and the procedure is repeated from point (a).
(e) A global $\frac{\chi^2}{\nu}$ is finally evaluated by also considering the vertical array of measurements.

Therefore, given the previous assumptions, the simplified model and the algorithm just described, the final correction applied to the bolometric measurements is:

$$\alpha_{1f} = \prod_{i=1}^{\#_{\text{iter}}} \delta_i \alpha_1 \setminus \delta_i := \begin{cases} 0 \text{ if not needed} \\ \in (0,1) \text{ otherwise} \end{cases}. \tag{13}$$

To estimate the correction in equation (10), the line-averaged densities in the core (LID3 or LDE3 from ellipticity measurements [33]) and in the edge (LID4 or LDE4) from the interferometer/polarimeter diagnostics, as well as the length of the aforementioned chords (LEN3 and LEN4, respectively) have been used. Figure 2 shows the layout of the aforementioned interferometric chords.

The electron temperatures have been extracted from the ECE measurements at the radial position of the density chords at the height of the magnetic axis and rescaled by the minimum value assumed by the profile. Finally, the Z-effective has been estimated using the spectroscopic signals.

The 'core' and the 'edge' regions cited above cannot be rigidly defined. However, considering the radial position of the just cited chords on the equatorial plane, the 'core' region refers roughly to that bounded by the closed surface labelled by $\rho_{\text{pol}} \sim 0.2$ and the edge to the interval $\sim 0.87 \leqslant \rho_{\text{pol}} \leqslant \sim 0.9$. The latter typically extends to the top of the pedestal.

To conclude this section, even if a word of caution is in place because of the type of plasma equilibrium assumed to describe the radiative behaviour of the plasma and to obtain equation (10), both the ERC correction and the methodology applied properly correct the contaminated data and, therefore, the assumptions made appear to be sufficient for the investigation carried out.

In the next section, the above procedure is applied to a few exemplificative time instances, and the implications on different physics interpretations are described.

4. Application of the methodology to experimental data

The methodology described in the previous section has been tested on a dataset from different DTE2 experiments, including baseline and hybrid scenarios. In figure 4, two instances for the pulse #99643, devoted to detecting alpha heating by delayed response of the electron temperature to ICRH modulation, are provided, and both are compared to the uncorrected or contaminated cases. Considering figures 4(A) and (B) at 8.05 s, at which the electron temperature is not hollow, w.r.t. figures 4(C) and (D), it is interesting to observe how the relative percentage of the core radiation (up to $\psi = 1$) over the total radiated power $\left(\text{i.e.} P_{\text{core}}/P_{\text{tot}}^{\text{rad}}\right)$ changes from 68% in the corrected case to 76% in the uncorrected case. Consequently, the relative change in the power outside the separatrix, i.e. in the scrape-off layer and in the divertor $\left(1 - \frac{P_{\text{core}}}{P_{\text{rad}}}\right)$ varies from 32% to 24% in the corrected and contaminated cases, respectively. Similar changes also occurred in other pulses and, therefore, the importance of the ERC correction for

an accurate estimate of the radiated fraction in detached discharges is evident. At the same time, the radiative blob at the edge in figure 4(D) is an overestimate of the actual emissivity and could lead to a wrong assessment of the relative importance of heavy impurities, such as W, usually emitting asymmetrically on the low-field side region, w.r.t. light ones like Ne, for example, usually emitting more in the divertor region [34].

With regard to figures 4(G), (H) and (I)–(L), both at 10.55 s, it has to be stated that there is no appreciable change in the relative percentages of the radiated power from the core w.r.t. the total radiated one in both cases considered. A similar situation has been observed for the relative percentages of the radiation outside the separatrix. Instead, the magnitude of the radiative power changes significantly also in this case as $\frac{P_{\text{core}}^{\text{corrected}}}{P_{\text{core}}^{\text{contaminatd}}} \sim 40\%$; $\frac{P_{\text{SOL+DIV}}^{\text{corrected}}}{P_{\text{SOL+DIV}}^{\text{contaminated}}} \sim 60\%$.

This is due to the shape of the emissivity, more localized in the edge and on top of the divertor as it can be appreciated by comparing figure 4(H) w.r.t. figure 4(L). Therefore, the relative integrals of the radiated powers in such regions w.r.t. the total radiated power do not change sensibly, but different conclusions could be drawn based on the shape of the emission profiles.

The examples reported thus show the importance of a dedicated correction to contaminated measurements, which might affect unsupervised algorithms.

It is out of the scope of this article to go into the details of the transport of heavy impurities [14] but, as an exemplificative application, the methodology described, it is worth mentioning that an important achievement for the performance of a discharge in terms of confinement lies in the so called 'impurity screening', i.e. in the effective capability to prevent heavy impurities from accumulating in the core [34]. An optimized density radiation profile would also have a direct impact in this case. Assuming in fact that the radiated power can be thought of as due to the radiative cooling of impurities, it is possible to write the radiation density of the plasma as [35]:

$$\rho_{\text{rad}}\left(n_e, n_i, T_e\right) = n_e \sum_{i=1}^{\#\text{ of species}} n_i L_i\left(T_e\right) \tag{14}$$

where the term L_i stands for the so-called 'cooling factor' [36] of the species 'i', which can be estimated by dedicated analysis based on structure codes [36]. In equation (14) n_e stands for the electron density and n_i stands for the ion densities of the species 'i'.

Therefore, by making specific assumptions about the emissivity, it is possible to estimate the density profiles of selected impurities [37].

On JET, in the first approximation W dominates the radiated power [26, 37] and, therefore, by dropping all terms in equation (14), except that due to W, it is possible to derive its density profile. Because of the assumptions made, the W profiles reported in figure 6(F) should be considered with great care. In figure 6(G), the profile related to the error committed by using the contaminated measurements instead of the corrected ones has also been reported. As can be observed,

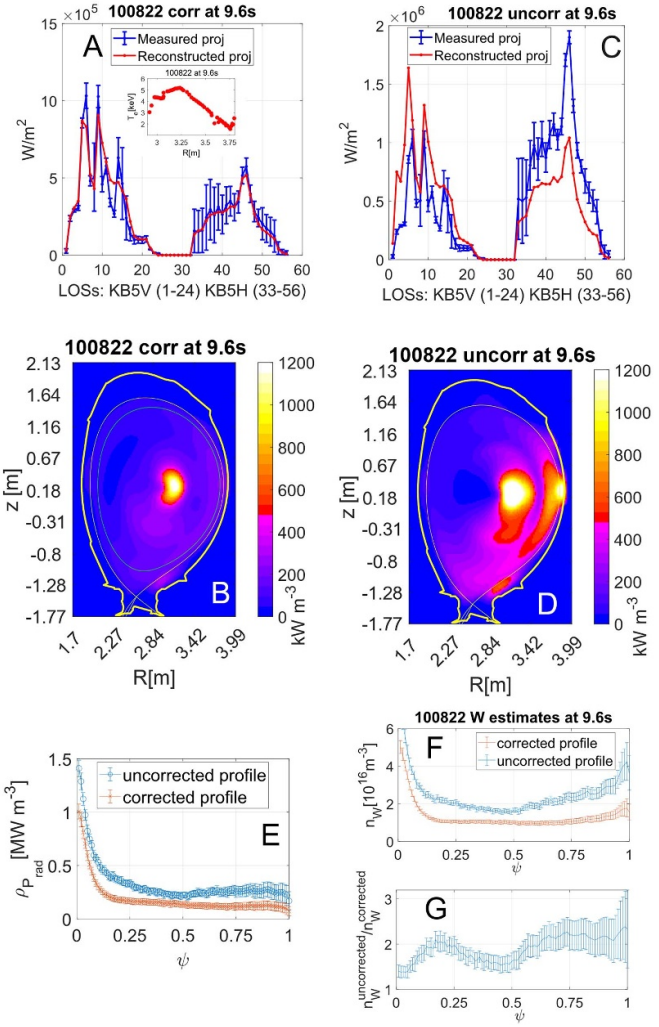

Figure 6. Discharge 100 822 in DD: measured and back-calculated projection once the correction ERC $\left(\alpha_{lf}^{100822}\left(t = 9.6\,\text{s}\right) \simeq 0.30\right)$ has been applied with the corresponding tomogram (A), (B) or not (C), (D). The hollow electron temperature profile has been reported in this case in (A); radiation density profiles for the two cases at the time instance considered in (E); (F): the estimates of the W concentration, with and without considering the correction. (G) Relative error performed without correcting the measurements. In this case it is evident how in both the intermediate region ($\psi \sim 0.2$) and up to the pedestal, the overestimate goes from ∼1.6 to ∼3.0. The last two points of the profile should not be considered because they are close to the limits of validity of the cooling factor used [36]. The main plasma parameters in terms of I_p, B_t, (n_e^c, T_e^c) and (n_e^e, T_e^e) are reported: 100822 : $[(2.5\,\text{MA}, 3.4\,\text{T}\ ,$ $\left(5.0 \cdot 10^{19}\text{m}^{-3}, 3.4\,\text{keV}\right), \left(2.6 \cdot 10^{19}\text{m}^{-3}, 1.3\ \text{keV}\right))]$.

the greatest error would be both in the intermediate region and, in this exemplificative case, at the edge up to the pedestal. In figures 6(A) and (C) the corrected and contaminated projections, for the time instances considered with a hollow electron profile, are reported, each corresponding to the tomograms in figures 6(B) and (D), respectively. A last word of caution is in place since the points at $(\psi, T_e\,[\text{eV}]) := \{(0.99, 497 \pm 245), (1.0, 334 \pm 241)\}$ should not be considered as the electron temperature is close, within the uncertainties, to the validity limits of the cooling factor

used [36]. Uncertainties have been propagated by taking advantage of the peculiarity of the ML method and the outputs of the EX2GK routines [38] used to estimate the density and electron temperature profiles with the corresponding uncertainties. The power density profiles used to derive the just discussed W profiles and relative errors in figures 6(F) and (G), respectively, are also reported in figure 6(E).

5. Conclusions

This article is devoted to describing corrections to be applied to tomographic algorithms, such as the EM used to compute the ML, with the aim of dealing with an important effect breaking the toroidal symmetry assumed by the tomographic inversion, namely strong gas puffing.

On JET, the two arrays of bolometers are placed in two different octants and, in the recent DTE2 campaign, recurrent [13] contamination of the horizontal array of bolometers has been observed.

The study performed here has also been able to decouple the importance of GIM06 in contaminating the measurements, w.r.t. the other MCF valves located either close to or in the same octant as the horizontal array of bolometers.

Starting with a pure empirical correction based only on the relative flow rate puffed by the MCF valves, it has been possible to link the observed distortion to the plasma characteristics. Then, by constructing a simplified model, a general correction has been derived, based on the ratio of the emissivities in the core and in the edge. Finally, an iterative methodology has been devised to fine-tune the correction. The derived correction and the methodology described have been tested on a database of relevant DT and DD discharges, characterized by different scenarios, and proved to be general enough to be deployed systematically.

Relevant physical quantities are naturally derived from tomographic reconstructions and, therefore, an accurate and reliable estimate is necessary to perform transport studies, impurity screening, detachment estimates and power-balance calculations [39]. Similarly, disruption avoidance or mitigation studies, devoted to establishing a radiative chain of events in terms of the spatial localization of the emissivity in the main chamber or based on the total radiated power, are evidently affected [40, 41]. Finally, MHD mode analysis and MHD studies related to trapped impurities are also influenced [42]. The suggested correction can be estimated automatically in principle, and also applied in combination with the defined methodology to other iterative and supervised codes on other devices.

Data availability statement

The data cannot be made publicly available upon publication because they are owned by a third party and the terms of use prevent public distribution. The data that support the findings of this study are available upon reasonable request from the authors.

Acknowledgments

This work has been carried out within the framework of the EUROfusion Consortium, funded by the European Union via the Euratom Research and Training Programme (Grant Agreement No. 101052200—EUROfusion). Views and opinions expressed are however those of the author(s) only and do not necessarily reflect those of the European Union or the European Commission. Neither the European Union nor the European Commission can be held responsible for them. The authors recognize the efforts spent and the work done by the preparation teams to plan and perform the experimental discharges reported in this manuscript related to the DTE2 campaign: F Auriemma, C Challis, J Hobirk, A Kappatou, K Kirov, E Lerche, C Maggi, J Mailloux, P Mantica.

ORCID iDs

Emmanuele Peluso https://orcid.org/0000-0002-6829-2180
Andrea Murari https://orcid.org/0000-0002-3932-3865
Teddy Craciunescu https://orcid.org/0000-0002-0012-4260
Michela Gelfusa https://orcid.org/0000-0001-5158-7292

References

[1] Ingesson L C, Alper B, Chen H, Edwards A W, Fehmers G C, Fuchs J C, Giannella R, Gill R D, Lauro-Taroni L and Romanelli M 1998 Soft x-ray tomography during ELMs and impurity injection in JET *Nucl. Fusion* **38** 1675–94
[2] Craciunescu T, Peluso E, Murari A and Gelfusa M 2018 Maximum likelihood bolometric tomography for the determination of the uncertainties in the radiation emission on JET tokamak *Rev. Sci. Instrum.* **89** 053504
[3] Mlynar J, Craciunescu T, Ferreira D R, Carvalho P, Ficker O, Ficker G, Imrisek M and Svoboda J 2018 Current research into applications of tomography for fusion *J. Fusion Energy* **38** 458–66
[4] Odstrcil M, Mlynar J, Odstrcil T, Alper B and Murari A 2012 Modern numerical methods for plasma tomography optimisation *Nucl. Instrum. Methods Phys. Res.* A **686** 156–61
[5] Craciunescu T, Bonheure G, Kiptily V V, Murari A, Soare S, Tiseanu I and Zoitaau V 2008 The maximum likelihood reconstruction method for JET neutron tomography *Nucl. Instrum. Methods Phys. Res.* A **595** 623–30
[6] Craciunescu T, Bonheure G, Kiptily V V, Murari A, Soare S, Tiseanu I and Zoitaau V 2009 A comparison of four reconstruction methods for JET neutron and gamma tomography *Nucl. Instrum. Methods Phys. Res.* A **605** 374–83
[7] Gelfusa M, Craciunescu T, Peluso E, Giacomelli L, Kiptily V, Reux C, Szepesi G and Murari A 2021 A maximum likelihood tomographic method applied to JET gamma ray emission during the current quench *Fusion Eng. Des.* **168** 112637
[8] Huber A *et al* 2007 Upgraded bolometer system on JET for improved radiation measurements *Fusion Eng. Des.* **82** 1327–34

[9] Adams J M, Jarvis O N, Sadlera G J, Symea D B and Watkins N 1993 The JET neutron emission profile monitor *Nucl. Instrum. Methods* A **329** 277–90

[10] Sertoli M *et al* (JET Contributors) 2018 Determination of 2D poloidal maps of the intrinsic W density for transport studies in JET-ILW *Rev. Sci. Instrum.* **89** 113501

[11] Matos F A, Ferreira D R and Carvalho P J 2017 Deep learning for plasma tomography using the bolometer system at JET *Fusion Eng. Des.* **114** 18–25

[12] Carvalho I S *et al* 2017 Operational aspects of the JET tritium introduction modules *Fusion Eng. Des.* **124** 841–5

[13] Carvalho P and Puglia P Influence of GIM7/TIM7 and GIM3/15/TIM15 on bolometer signals and tomography (available at: https://users.euro-fusion.org/pages/tfiospti/TFmeetings/2019/20190221/PCarvalho_tf_BoloGim7.3.pdf)

[14] Angioni C 2021 Impurity transport in tokamak plasmas, theory, modelling and comparison with experiments *Plasma Phys. Control. Fusion* **63** 073001

[15] Hawryluk R J *et al* 1980 An empirical approach to tokamak transport *Physics of Plasmas Close to Thermonuclear Conditions* ed B Coppi (Brussels: CEC) pp 19–46

[16] Huber A *et al* 2007 Improved radiation measurements on JET—first results from an upgraded bolometer system *J. Nucl. Mater.* **363** 365–70

[17] Craciunescu T *et al* submitted to Plasma Physics and Controlled Fusion

[18] Shepp L A and Vardi Y 1982 Maximum likelihood emission tomography *IEEE Trans. Med. Imaging* **1** 113–22

[19] Lange K and Carson K 1984 EM reconstruction algorithms for emission and transmission tomography *J. Comput. Assist. Tomogr.* **8** 306–16

[20] Barrett H H, Wilson D W and Tsui B M W 1994 Noise properties of the EM algorithm I. Theory *Phys. Med. Biol.* **39** 833–46

[21] Li Y 2011 Noise propagation for iterative penalized-likelihood image reconstruction based on Fisher information *Phys. Med. Biol.* **56** 1083–103

[22] R L S 2010 *Poisson Point Processes Imaging, Tracking, and Sensing* (New York: Springer) (https://doi.org/10.1007/978-1-4419-6923-1)

[23] Peluso E, Gelfusa M, Craciunescu T, Martellucci L, Gaudio P, Carvalho P and Murari A 2022 Dealing with artefacts in JET iterative bolometric tomography using masks *Plasma Phys. Control. Fusion* **64** 045013

[24] Peluso E, Craciunescu T, Murari A, Carvalho P J and Gelfusa M 2019 A comprehensive study of the uncertainties in bolometric tomography on JET using the maximum likelihood method *Rev. Sci. Instrum.* **90** 123502

[25] Peluso E, Craciunescu T, Gelfusa M, Murari A, Carvalho P J and Gaudio P 2019 On the effects of missing chords and systematic errors on a new tomographic method for JET bolometry *Fusion Eng. Des.* **146** 2124–9

[26] Ivanova-Stanik I, Challis C D, Chomiczewska A, Hobirk J, Huber A, Kappatou A, Lerche E, Telesca G and Zag´orski R 2022 Influence of the impurities in the hybrid discharges with high power in JET ILW *Nucl. Fusion* **62** 066010

[27] Stankiewicz R and Zagórski R 2003 Effect of core-edge coupling on operation regimes of ITER-like reactor *J. Nucl. Mater.* **313–6** 899–903

[28] Jaulmes F, Zadvitskiy G, Bogar K, Imrisek M, Hromadka J, Cats S Y, Varju J, Komm M and Panek R 2021 Modelling of charge-exchange induced NBI losses in the COMPASS upgrade tokamak *Nucl. Fusion* **61** 046012

[29] Dux R, Cavedon M, Kallenbach A, McDermott R M and Vogel G 2020 Influence of CX-reactions on the radiation in the pedestal region at ASDEX Upgrade *Nucl. Fusion* **60** 126039

[30] Ingesson L C, Alber B, B J P and Vallet J C 2008 Chapter 7 tomography diagnostics: bolometry and soft-x-ray detection *Fusion Sci. Technol.* **53** 528–76

[31] Stratton B C, Bitter M, Hill K W, Hillis D L and Hogan J T 2008 Chapter 5 passive spectroscopic diagnostics for magnetically confined fusion plasmas *Fusion Sci. Technol.* **53** 431–86

[32] Von Goeler S, Stodiek W, Eubank H, Fishman H, Grebenshchikov S and Hinnov E 1975 Thermal x-ray spectra and impurities in the ST tokamak *Nucl. Fusion* **15** 301

[33] Rossi R, Boboc A, Orsitto F P, Gelfusa M and Gaudio P 2021 First measurements of line-integrated electron density in an ITER-like configuration using the JET far infrared polarimeter diagnostic *Plasma Phys. Control. Fusion* **63** 4

[34] McCracken G M, Lipschultz B, LaBombard B, Goetz J A, Granetz R S, Jablonski D, Lisgo S, Ohkawa H, Stangeby P C and Terry J L 1997 Impurity screening in ohmic and high confinement (H-mode) plasmas in the Alcator C-Mod tokamak *Phys. Plasmas* **4** 1681–9

[35] Goldston R J, Reinke M L and Schwartz J A 2017 A new scaling for divertor detachment *Plasma Phys. Control. Fusion* **59** 055015

[36] Putterich T, Neu T, Dux R, Whiteford A D, O'Mullane M G and H P S 2010 Calculation and experimental test of the cooling factor of tungsten *Nucl. Fusion* **50** 025012

[37] Field A R *et al* 2023 Peripheral temperature gradient screening of high-Z impurities in optimised 'hybrid' scenario H-mode plasmas in JET-ILW *Nucl. Fusion* **63** 016028

[38] A H, Citrin J, Auriemma F, Bourdelle C, Casson F J, Kim H-T, Manas P, Szepesi G and Weisen H 2019 Application of Gaussian process regression to plasma turbulent transport model validation via integrated modelling *Nucl. Fusion* **59** 056007

[39] Murari A, Peluso E, Craciunescu T, Lowry C, Aleiferis S, Carvalho P and Gelfusa M 2020 Investigating the thermal stability of highly radiative discharges on JET with a new tomographic method *Nucl. Fusion* **60** 046030

[40] Vega J, Murari A, Dormido-Canto S, Rattá G A and Gelfusa M 2022 Disruption prediction with artificial intelligence techniques in tokamak plasmas *Nat. Phys.* **18** 741–50

[41] Murari A, Rossi R, Lungaroni M, Baruzzo M and Gelfusa M 2021 Stacking of predictors for the automatic classification of disruption types to optimize the control logic *Nucl. Fusion* **61** 036027

[42] Hender T C *et al* 2016 The role of MHD in causing impurity peaking in JET hybrid plasmas *Nucl. Fusion* **56** 066002